# Preparation and X-ray Structures of Metal-Free, Dicobalt and Dimanganese Forms of Soluble Methane Monooxygenase Hydroxylase from *Methylococcus capsulatus* (Bath)†

Matthew H. Sazinsky, Maarten Merkx, Elisabeth Cadieux, Sonya Tang, and Stephen J. Lippard*

*Department of Chemistry, Massachusetts Institute of Technology, Cambridge, Massachusetts 02139*

*Received August 28, 2004; Revised Manuscript Received October 5, 2004*

ABSTRACT: A three-component soluble methane monooxygenase (sMMO) enzyme system catalyzes the hydroxylation of methane to methanol at a carboxylate-bridged diiron center housed in the α-subunit of the hydroxylase (MMOH). Catalysis is facilitated by the presence of a regulatory protein (MMOB) and inhibited by MMOD, a protein of unknown function encoded in the sMMO operon. Both MMOB and MMOD are presumed to bind to the same region of the MMOH α-subunit. A colorimetric method for monitoring removal of Fe(II) from MMOH was developed using 1,10-phenanthroline and yields apo MMOH with <0.1 Fe/homodimer. With the use of this method, it was possible to investigate the X-ray structure of the apoenzyme and to perform metal reconstitution studies. Using MMOH from *Methylococccus capsulatus* (Bath), the effects of MMOB and MMOD on metal binding were studied and structural perturbations relevant to the function of this enzyme were identified. X-ray crystal structures of the apo, Mn(II)-soaked, and Co(II)-grown MMOH, determined to 2.3 Å or greater resolution, reveal that the presence of metal ions is essential for the proper folding of helices E, F, and H of the α-subunit. The active sites of Mn(II)-soaked and Co(II)-grown MMOH are similar to that of reduced, native MMOH with notable differences in the metal−metal distances and ligand coordination sphere that may reflect how this dinuclear metal center might change in the presence of MMOB. MMOB and MMOD decrease the rate of removal of Fe(II) from the enzyme by 22- and 16-fold, respectively. On the basis of previous studies, it is hypothesized that MMOB, and perhaps MMOD, function to block solvent access to the MMOH active site. Finally, ITC studies and the observed disorder in helices E, F, and H in the apo and Mn(II)-soaked structures suggest that these regions of MMOH are critical for MMOB and MMOD binding.

The hydroxylase protein (MMOH)[1] of soluble methane monooxygenase (sMMO) from *Methylococcus capsulatus* (Bath) harbors a non-heme, carboxylate-bridged diiron center within a four-helix bundle that catalyzes the oxidation of methane to methanol (*1*). This reaction is the first in a metabolic pathway that enables methanotrophic bacteria to utilize methane as a sole source of energy and carbon (eq 1).

$$CH_4 + O_2 + NADH + H^+ \rightarrow CH_3OH + H_2O + NAD^+ \quad (1)$$

In addition to MMOH, two other proteins, MMOR and MMOB, are required for catalysis. MMOR is a flavin- and ferredoxin-containing reductase that transfers electrons obtained from NADH via its ferredoxin domain to reduce the diiron center in MMOH to the Fe(II)Fe(II) oxidation state. At this oxidation level, MMOH can react with dioxygen to form several activated oxygen intermediates, but only in the presence of a 16 kDa cofactorless regulatory protein, MMOB. Two of these intermediates, a peroxo-bridged diiron(III) species ($H_{peroxo}$) and an oxo-bridged diiron(IV) complex (Q), have been studied extensively by using a variety of time-resolved spectroscopic techniques and density functional theoretical (DFT) calculations (*1*, *2*). As the diiron center proceeds through the different intermediates during the course of the reaction, the Fe−Fe distance and the positions of the bridging carboxylates change to accommodate different oxidation states, substrate binding, and substrate activation (Scheme 1). Recently, a fourth protein component within the soluble methane monooxygenase operon, MMOD, was identified in cells expressing sMMO and found to inhibit catalysis by binding to the MMOH α-subunit with an affinity similar to that of MMOB and MMOR (*3*). The function of the 11 kDa MMOD protein is still unclear, but it has been

† This research was supported by National Institute of General Medical Sciences Grant GM32134 (S.J.L.). M.H.S. was an NIH Biotechnology Grant GM08334 trainee. M.M. was a Human Frontier of Science Program Postdoctoral Fellow. E.C. was funded by le Fonds Québécois de Recherche sur la Nature et les technologies. S.T. was an MIT Undergraduate Research Opportunities Participant.

* To whom correspondence should be addressed. Telephone: (617) 253-1892. Fax: (617) 258-8150. E-mail: lippard@mit.edu.

[1] Abbreviations: BMM, bacterial multicomponent monooxygenase; sMMO, soluble methane monooxygenase; MMOH, methane monooxygenase hydroxylase; MMOB, methane monooxygenase effector protein; MMOR, methane monooxygenase reductase; MMOD, methane monooxgenase *orfY* gene product; RNR-R2, class I ribonucleotide reductase R2 subunit; MOPS, 3-(*N*-morphilino)propanesulfonic acid; DFT, density functional theory; XAS, X-ray absorption spectroscopy; MCD, magnetic circular dichroism; CD, circular dichroism; ITC, isothermal titration calorimetry; ToMO, toluene/*o*-xylene monooxygenase; ToMOH, toluene/*o*-xylene monooxygenase hydroxylase; T4MO, toluene 4-monooxygenase; TCEP, tris(2-carboxyethyl)phosphine; $MMOH_{ox}$, oxidized MMOH; $MMOH_{red}$, reduced MMOH.

10.1021/bi048140z CCC: $27.50 
Published on Web 12/04/2004

Scheme 1: Proposed Reaction Cycle of sMMO

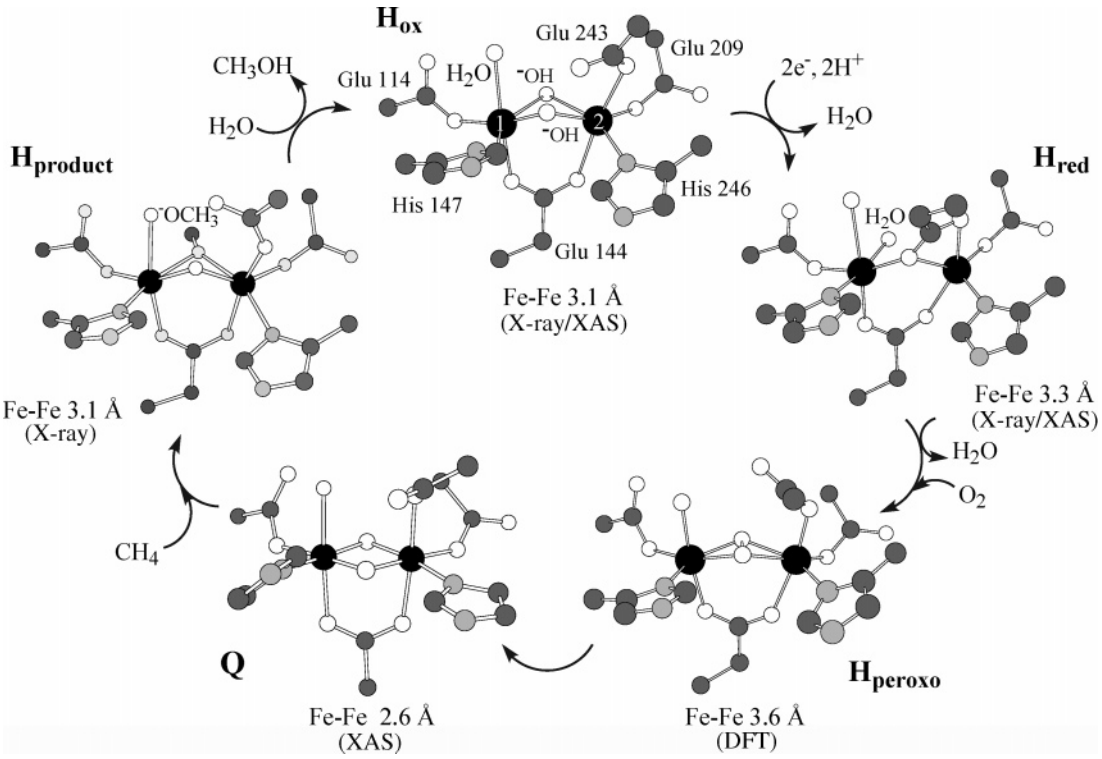


hypothesized to be involved in the folding of MMOH and assembly of the diiron center in vivo.

Several four-helix bundle, non-heme diiron proteins, including MMOH, the R2 subunit of type I ribonucleotide reductase (RNR-R2), hemerythrin, and bacterioferritin, can be converted to their apo forms, from which various metal-substituted derivatives have been prepared (*4*−*11*). Structural studies of the apoproteins have been useful in probing the contributions of divalent metal ions to the proper folding of the native forms (*6*, *10*, *12*−*14*).

Structural and spectroscopic studies of the metal-reconstituted apoproteins provided insight into their active site geometries and helped to identify alternate metal−ligand interactions that may be relevant to catalysis and function (*4*−*11*). Cobalt(II) and manganese(II) have been the most attractive candidates for replacing the native iron in these proteins. Both are similar to iron(II) in charge and ionic radius and have attractive optical ($Co^{2+}$) and magnetic ($Co^{2+}$ and $Mn^{2+}$ are EPR-active) properties that allow their binding geometries to be investigated. In addition, both can exist in different oxidation states. Stable peroxo- and superoxo-bridged dicobalt(III) centers are well-known (*15*) and, if formed in the MMOH active site, could provide valuable information regarding the structure of the $H_{peroxo}$ intermediate. Stable high-valent dimanganese centers such as Mn(III)Mn(IV) and Mn(IV)Mn(IV) have precedent in both synthetic analogues and metalloenzymes (*16*, *17*). If formed in manganese-reconstituted MMOH, they could provide a model for high-valent intermediates such as Q in sMMO and X in RNR-R2. Dimanganese(II) derivatives have been prepared for ribonucleotide reductase (*4*, *8*, *18*), hemerythrin (*10*, *18*), and methane monooxygenase (*5*). The X-ray structure reported for manganese-substituted *Escherichia coli* RNR-R2 in the Mn(II)Mn(II) oxidation state proved to be a good mimic of the chemically and photoreduced enzyme, whereas the mixed-valent Mn(II)Mn(III) structure identified a novel iron ligand conformational change in one of the coordinated Glu ligands. Both structures contributed to a mechanistic understanding of $O_2$ activation and tyrosyl radical generation in RNR (*4*, *8*). Dicobalt(II) forms have also been reported for ribonucleotide reductase (*7*), hemerythrin (*11*), and bacterioferritin (*9*), allowing them to be characterized by optical spectroscopy. The structure of dicobalt(II)-reconstituted mouse RNR-R2 exhibited metal ligand conformations that were not previously observed in the active sites of these enzymes. The dicobalt(II) structure resembled more closely that of the reduced MMOH diiron center than reduced *E. coli* RNR-R2 (*19*). The dimanganese(II) and dicobalt(II) metal-substituted forms of RNR did not react with dioxygen (*7*, *18*). The dicobalt(II) complexes were also unreactive toward hydrogen peroxide.

In this article, we report a new method for preparing apo MMOH from the native enzyme in nearly quantitative yield. The apoprotein is stable, and upon addition of $Fe(NH_4)_2(SO_4)\cdot 6H_2O$, MMOH regains most of its native activity. The availability of apo MMOH allowed us to prepare cobalt- and manganese-reconstituted forms of MMOH. The X-ray crystal structures of apo MMOH and derivatives with dinuclear Co(II) and dinuclear Mn(II) centers were determined. The results provide new insight into the geometric flexibility of the carboxylate-bridged dimetallic centers and the contribution of the coordinated metal ions to the folding and stability of the four-helix bundle that houses them. These results also suggest possible effects of MMOB and MMOD on the hydroxylase protein.

## EXPERIMENTAL PROCEDURES

*Materials and General Methods.* MMOH was purified from *M. capsulatus* (Bath) as previously described (*3*, *20*).

Purified MMOH contained 3.5−4.0 Fe atoms/dimer and catalyzed the epoxidation of propylene with a rate of 0.35 $s^{-1}$ (250 mU/mg) at 25 °C. MMOB (*21*), MMOR (*22*), and MMOD (*3*) were obtained from recombinant expression systems in *E. coli* as described previously. Iron analysis was performed by using a ferrozine assay (*23*).

*Kinetics of Release of Iron from $MMOH_{red}$.* A solution of 100 $\mu$M MMOH in 25 mM MOPS (pH 7.0), 120 mM NaCl, 100 $\mu$M methyl viologen, and 5% (v/v) glycerol was made anaerobic by repeated vacuum/$N_2$ cycles. Sodium dithionite was added to a final concentration of 5 mM, and the solution was incubated for at least 30 min to allow full reduction of the MMOH diiron centers. A Thünberg cuvette filled with 1.8 mL of 25 mM MOPS (pH 7.0), 120 mM NaCl, and 2 mM 1,10-phenanthroline was made anaerobic by repeated vacuum/$N_2$ cycles, and sodium dithionite was added to a final concentration of 5 mM. The cuvette was mounted in a HP8354 diode array spectrophotometer (Hewlett-Packard), and the reaction was started by anaerobic addition of 200 $\mu$L of the $MMOH_{red}$-containing solution to the cuvette (final concentration, 10 $\mu$M). The formation of $[Fe(o\text{-phen})_3]^{2+}$ was monitored at 510 nm ($\epsilon$ = 11 100 $M^{-1}$ $cm^{-1}$) for 8−36 h at 25 °C. Reactions in the presence of MMOD and MMOB were performed in the same manner by adding either protein (220 $\mu$M) to the 100 $\mu$M MMOH solution prior to reduction by dithionite.

*Preparation of Apo MMOH.* A 2 mL solution of 0.2 mM MMOH, 4 mM 1,10-phenanthroline, 1 mM methyl viologen in 25 mM MOPS (pH 7.0), 120 mM NaCl, and 5% glycerol was made anaerobic in a glass vial with a rubber septum by repeated vacuum/$N_2$ cycles. A 20 $\mu$L aliquot of an anaerobic 400 mM sodium dithionite solution was added, and the reaction mixture was incubated at room temperature for 5 h. Apo MMOH was separated from these reagents and the $[Fe(o\text{-phen})_3]^{2+}$ complex by using an EconoPac 10DG (Bio-Rad) disposable desalting column equilibrated with a buffer containing 25 mM MOPS (pH 7.0), 120 mM NaCl, and 5% glycerol. Fractions containing apo MMOH were identified by their absorption at 280 nm, pooled, concentrated, and stored at −80 °C.

*Preparation of Iron-Reconstituted MMOH.* Apo MMOH (240 $\mu$M) was made anaerobic by purging under vacuum with $N_2$ in a buffer comprising 25 mM MOPS (pH 7.0), 100 mM NaCl, and 5% glycerol and brought into an anaerobic chamber. A solution of $Fe(NH_4)_2(SO_4)_2{\cdot}6H_2O$ (final concentration, 4 mM) was added to the protein in the presence of 2 mM dithionite and 50 $\mu$M methyl viologen. After being incubated overnight at room temperature, the protein was dialyzed against 2 × 600 mL changes of an anaerobic solution of 25 mM MOPS (pH 7.0), 120 mM NaCl, 5% glycerol, 1 mM methyl viologen, and 2 mM dithionite for 3 h to remove excess iron. The method yielded 3.4−3.5 Fe atoms/MMOH.

*Activity Assays.* The activity of sMMO was assayed by monitoring the formation of propylene oxide from propylene by gas chromatography or consumption of NADH ($\epsilon_{340}$ = 6220 $M^{-1}$ $cm^{-1}$) by UV−vis spectroscopy essentially as described previously (*3*, *24*).

*Kinetics of Iron Reconstitution of Apo MMOH.* Iron reconstitution of apo MMOH was performed as described previously with the following changes (*3*). The reconstitution reaction was carried out under aerobic and anaerobic conditions; the latter employed a septum-sealed glass vial made anaerobic by repeated vacuum/nitrogen cycles. Apo MMOH (47.5 $\mu$M) was incubated with 0.5 mM $Fe(NH_4)_2(SO_4)_2{\cdot}6H_2O$ in 25 mM MOPS (pH 7.0), 120 mM NaCl, 2 mM DTT, and 5% (v/v) glycerol at 25 °C. At several time points after the iron solution had been added, samples were taken and assayed for propylene activity by gas chromatography as described above. The effect of the iron concentration on the kinetics of iron reconstitution was studied by anaerobic incubation of 35 $\mu$M apo MMOH with 1.48, 0.49, and 0.15 mM $Fe(NH_4)_2(SO_4)_2{\cdot}6H_2O$ in 25 mM MOPS (pH 7.0), 120 mM NaCl, 2 mM DTT, and 5% (v/v) glycerol, at 25 °C. Aliquots were taken at various time points, and the MMO activity was assayed at 25 °C by using propylene as a substrate and monitoring the concentrations of NADH at 340 nm.

*Isothermal Titration Calorimetry.* Calorimetric experiments were performed by using a VP-ITC titration calorimeter (Microcal). All protein samples were exchanged by dialysis at 4 °C into a buffer comprising 25 mM MOPS (pH 7.0) and 5% glycerol before being used. Tris(2-carboxyethyl)phosphine (TCEP) (1 mM) was added to all buffers in which MMOD was present. The reaction cell contained 1.4 mL of holo or apo MMOH at a concentration of 15 $\mu$M. The injection syringe was filled with 250 $\mu$M MMOD or 313 $\mu$M MMOB and was rotating at 310 rpm during the titration. The titration experiments consisted of 40 injections, 6 $\mu$L each for a duration of 6 s with 420 s intervals between injections. The temperature during the titration was kept at 20 °C. The data were analyzed by using software provided by Microcal.

*Optical Spectroscopy of Co(II)-Bound MMOH.* Apo MMOH was centrifuged at 14000*g* for 30 min immediately before addition of cobalt(II) chloride to remove small amounts of the denatured protein that would otherwise make the observation of the very weak Co(II) d−d transitions difficult. A cuvette was filled with 450 $\mu$L of a 105 $\mu$M apo MMOH solution in 25 mM MOPS (pH 7.0), 120 mM NaCl, and 5% (v/v) glycerol, and the spectra were recorded. A small aliquot of a 10 mM $CoCl_2$/0.1 mM HCl stock solution was added, and a second spectrum was recorded after re-equilibration. After correction for dilution, a difference spectrum was calculated by subtracting the apo MMOH spectrum from that of the Co-containing solution.

*CD Spectroscopy of Holo and Apo MMOH.* Samples of apo and holo MMOH for circular dichroism analysis contained 10 mM potassium phosphate (pH 7.0) and 0.1 $\mu$M hydroxylase. Spectra were recorded on an Aviv CD spectrophotometer at 25 °C and were the average of five scans.

*Crystallization of Apo MMOH and Its Mn(II) and Co(II) Derivatives.* Apo, Co(II)-substituted, and Mn(II)-substituted MMOH were crystallized at 4 °C by using a method similar to those previously published with the following modifications (*25*). Well solutions contained 160 mM MOPS (pH 7.0), 350 mM $CaCl_2$, 10% (w/w) PEG 8000, and 0.015% $NaN_3$. Protein drops contained 3 $\mu$L of 40 $\mu$M apo MMOH in 25 mM MOPS (pH 7.0), 1.5 $\mu$L of well solution, and 1.5 $\mu$L of an MMOH microseed solution prepared in the mother liquor. Mn(II)- and Co(II)-reconstituted MMOH were created by crystallizing apo MMOH in the presence of 10−20 mM $MnCl_2$ or $CoCl_2$ or soaking apo MMOH crystals for 30 min in a cryosolution comprising 160 mM MOPS (pH 7.0), 350 mM $CaCl_2$, 10% (w/w) PEG 8000, 25% (v/v) glycerol, and

Table 1: Data Collection and Refinement Statistics

| | apo MMOH | Mn(II) MMOH | Co(II) MMOH |
|---|---|---|---|
| | Data Collection | | |
| beamline | SSRL 9-1 | SSRL 7-1 | SSRL 7-1 |
| wavelength (Å) | 1.00 | 1.08 | 1.08 |
| space group, *Z* | $P2_12_12_1$, 4 | $P2_12_12_1$, 4 | $P2_12_12_1$, 4 |
| unit cell dimensions (Å) | | | |
| *a* | 70.35 | 70.92 | 71.44 |
| *b* | 171.62 | 171.67 | 171.84 |
| *c* | 221.01 | 220.27 | 220.93 |
| resolution range (Å) | 30−2.1 | 30−2.3 | 30−2.1 |
| no. of total reflections | 607337 | 289572 | 584441 |
| no. of unique reflections | 156085 | 117119 | 159323 |
| completeness (%)[a] | 92.2 (88.3) | 91.7 (90.7) | 97.7 (90.4) |
| $I/\sigma(I)$ | 13.6 (3.1) | 11.3 (2.8) | 12.2 (2.9) |
| $R_{sym}$ (%)[b] | 6.9 (43.5) | 5.8 (29.5) | 5.7 (38.8) |
| | Refinement | | |
| $R_{cryst}$ (%)[c] | 22.3 | 21.1 | 19.4 |
| $R_{free}$ (%)[d] | 26.5 | 25.9 | 22.5 |
| no. of atoms | | | |
| protein | 17312 | 17317 | 17325 |
| water | 795 | 1116 | 847 |
| rmsd for bond lengths (Å) | 0.0061 | 0.0060 | 0.0061 |
| rmsd for bond angles (deg) | 1.194 | 1.161 | 1.18 |
| average *B*-factor (Å$^2$) | 40.0 | 42.6 | 37.7 |

[a] Values in parentheses are for the highest-resolution shell. [b] $R_{sym} = \sum_i\sum_{hkl}|I_i(hkl) - \langle I(hkl)\rangle|/\sum_{hkl}\langle I(hkl)\rangle$, where $I_i(hkl)$ is the *i*th measured diffraction intensity and $\langle I(hkl)\rangle$ is the mean of the intensity for the Miller index (*hkl*). [c] $R_{cryst} = \sum_{hkl}||F_o(hkl)| - |F_c(hkl)||/\sum_{hkl}|F_o(hkl)|$. [d] $R_{free} = R_{cryst}$ for a test set of reflections (5% in each case).

50 mM $MnCl_2$ or $CoCl_2$. Cystals of apo MMOH did not grow well in the presence of $MnCl_2$.

*X-ray Diffraction Data Collection and Structure Refinement.* Data sets were collected at the Stanford Synchrotron Radiation Laboratory (SSRL) on beam lines 9-1 and 7-1. MOSFLM (*26*) was used to determine a collection strategy with knowledge of the space group ($P2_12_12_1$) and the unit cell (70 Å × 171 Å × 222 Å). Data sets were collected at 100 K with a 0.5° oscillation over a 100−120° rotation of the crystal. The HKL suite of programs was used to index and scale the data (*27*). The scaling and refinement statistics for the apo, Co(II)-grown, and Mn(II)-soaked apo MMOH structures are listed in Table 1.

The initial phases were determined by rigid body refinement in CNS (*28*) using a starting model in which the iron and the metal-coordinating ligands were removed. The protein models were built in XtalView (*29*) and refined by using CNS. PROCHECK was used to check the final model geometry and statistics (*30*). The atomic coordinates and structure factors for the apo, Mn(II)-soaked, and Co(II)-grown MMOH structures have been deposited as entries 1XMG, 1XMF, and 1XMH, respectively, in the Protein Data Bank.

## RESULTS

*Generation of Apo MMOH.* A previously reported method for the preparation of apo MMOH used 3,4-dihydroxybenzaldehyde to extract the ferric ions from the active sites of the resting enzyme (*5*). The ferric complex of this ligand remains bound to the protein, and the addition of a second chelating agent, 8-hydroxyquinolinesulfonate, is required to prepare iron-depleted MMOH. In our hands, this method did yield preparations with ~0.2 Fe/MMOH, but the procedure also resulted in the formation of a brown color that was not removed easily by anion exchange or size exclusion chromatography.

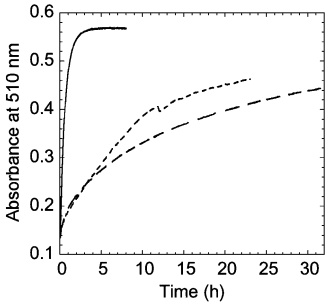


FIGURE 1: Kinetics iron release from $MMOH_{red}$ in the presence of 1,10-phenanthroline as monitored by the formation of $[Fe(o\text{-phen})_3]^{2+}$ at 510 nm. The reaction was carried out anaerobically as described in the text in the presence or absence of 22 $\mu$M MMOD or 22 $\mu$M MMOB: (—) $MMOH_{red}$ only, (- - -) $MMOH_{red}$ and MMOD, and (— — —) $MMOH_{red}$ and MMOB.

Extraction of iron from iron-binding proteins is often easier when the metal ion is reduced to $Fe^{2+}$, for which ligand exchange rates are more rapid compared to those for $Fe^{3+}$ (*31*). To test whether this property also holds for MMOH, the enzyme was reduced by the addition of excess sodium dithionite and methyl viologen. An aliquot was then transferred anaerobically to a cuvette containing the strong $Fe^{2+}$ chelator 1,10-phenanthroline, and the formation of the red/orange $[Fe(o\text{-phen})_3]^{2+}$ complex was monitored by optical spectroscopy at 510 nm ($\epsilon_{510}$ = 11 100 $M^{-1}$ $cm^{-1}$). Figure 1 shows that formation of the tris(phenanthroline)iron(II) complex is complete after approximately 3 h at 25 °C. A fit of the absorbance at 510 nm using a single exponential gave a rate constant of 1.6 $h^{-1}$ and the release of 3.8 Fe atoms per MMOH dimer. Excess reagents and the $[Fe(o\text{-phen})_3]^{2+}$ complex are easily separated from apo MMOH by using a desalting column. This new method gave colorless apo MMOH preparations with very little residual iron (<0.1 Fe/MMOH dimer) in 80−90% yield.

Both MMOB and MMOD affect the structure of the MMOH diiron sites (*3*). It has been demonstrated previously that MMOB can block the reconstitution of active MMOH from apo MMOH and $Fe(NH_4)_2(SO_4)\cdot 6H_2O$, but it is unclear whether MMOD inhibits iron uptake since activity assays were the method by which iron reconstitution was monitored and MMOD inhibits hydroxylase activity (*3*). To determine whether MMOB and MMOD affect the stability of $MMOH_{red}$, the reaction of the latter with 1,10-phenanthroline was repeated in the presence of 2.2 molar equiv of MMOB or MMOD (Figure 1). The release of $Fe^{2+}$ is severely inhibited by both proteins, the rate constants being 0.07 and 0.11 $h^{-1}$, respectively, for the two.

*Iron-Reconstituted MMOH.* The experimental procedure described above yields MMOH with ~3.4 Fe atoms/molecule. Mössbauer and EPR spectra of the oxidized and reduced reconstituted forms of MMOH were identical to those reported previously for the holoenzyme (data not shown) (*32*). This finding indicates that this procedure afforded properly assembled metal centers. Moreover, this reconstituted protein was approximately 80% as active as the wild-type enzyme, possibly because of its decreased iron content. Since MMOB slows the removal of iron from MMOH, its addition to the metal reconstitution buffer before

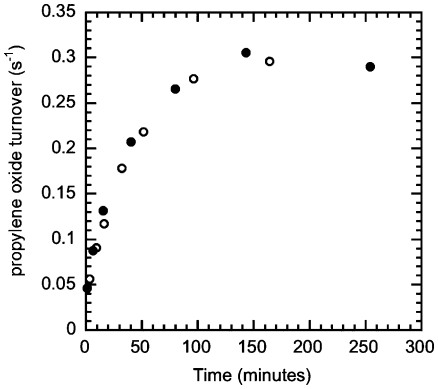


FIGURE 2: Kinetics of formation of active MMOH from apo MMOH and $Fe^{2+}$ at 25 °C under anaerobic (○) and aerobic conditions (●). MMOH activity asssays monitor the formation of propylene oxide by using gas chromatography as described in the text.

dialysis may increase the yield of hydroxylase containing a full complement of iron atoms.

*Reconstitution of Hydroxylase Activity.* Previous studies reported variable success in reconstitution of catalytically active MMOH from apo MMOH and iron salts (*5*, *33*). Figure 2 reveals that simple addition of excess $Fe(NH_4)_2(SO_4)\cdot 6H_2O$ to apo MMOH, either anaerobically or aerobically, restores the formation of active enzyme to the same level as native MMOH within 2 h at 25 °C. The rate of reconstitution depends on the iron concentration (Figure S1 of the Supporting Information). The observation that complete restoration of activity occurs upon incubation of apo MMOH with $Fe^{2+}$ demonstrates that the apoprotein is not irreversibly unfolded. Anaerobic addition of $Fe(NH_4)_2(SO_4)_2\cdot 6H_2O$ to apo MMOH also results in formation of the $g = 16$ signal typical of $MMOH_{red}$ (*1*), providing additional evidence that the native diiron center has been restored (not shown).[2]

*Isothermal Titration Calorimetry.* Several different experimental techniques have been used to determine the constants for binding of MMOB and MMOD to MMOH (*3*, *24*); however, no method has yet compared directly the relative affinities of these two proteins for apo and holo MMOH. Isothermal titration calorimetry (ITC) was therefore performed to assess the binding of MMOB and MMOD to the metalated and demetalated forms of the hydroxylase. The normalized binding isotherms and calculated titration curves are presented in Figure 3. The data were best fit by using a cooperative binding model in which two molecules of MMOB or MMOD were assumed to bind to MMOH with affinities $K_{d1}$ and $K_{d2}$ (eq 2), where H represents MMOH

$$H + X \overset{K_{d1}}{\rightleftharpoons} HX + X \overset{K_{d2}}{\rightleftharpoons} HX_2 \qquad (2)$$

and X either MMOB or MMOD. The calculated dissociation constants are presented in Table 2. These results clearly indicate that MMOB has a stronger affinity for holo MMOH than MMOD and that the latter binds more tightly to apo MMOH than does MMOB. The MMOB and MMOD binding constants for apo and holo MMOH, as determined by ITC, are consistent with the values derived from previous work (*3*, *24*).

[2] M. Merkx, J. Bautista, and S. J. Lippard, unpublished results.

*UV−Vis Spectroscopic Study of Cobalt-Substituted MMOH.* The availability of an efficient method for preparing apo MMOH with a low iron content and no contaminating chromophores allowed us to explore the coordination chemistry of the MMOH active site ligands. A dicobalt(II)-substituted form of MMOH was prepared. The optical spectroscopic bands of Co(II) contain valuable information about its coordination geometry (*34*). Octahedrally coordinated $d^7$ Co(II) complexes typically display visible absorption bands with extinction coefficients of 5−40 $M^{-1}$ $cm^{-1}$. Tetrahedral or pseudotetrahedral sites show much more intense d−d bands with extinction coefficients ranging from 200 to 800 $M^{-1}$ $cm^{-1}$, and five-coordinate sites have intensities that are somewhere between these values. For this reason, substitution with cobalt(II) is often used to probe the coordination properties of metal binding sites in proteins having spectroscopically silent metal ions such as $Zn^{2+}$ (*35*). Figure 4 shows difference spectra obtained after subtraction of the spectrum of apo MMOH from that of the apoprotein in the presence of 1, 2, and 4 molar equiv of $CoCl_2$. The spectra exhibit maximal absorption at 520 nm with an extinction coefficient of 35−40 $M^{-1}$ $cm^{-1}$. Addition of excess $CoCl_2$ resulted in additional spectral changes with a similar shape but a significantly lower extinction coefficient (7 $M^{-1}$ $cm^{-1}$) that is typical of aquated Co(II). Prolonged standing of the Co-containing MMOH solution in air did not lead to any spectral changes, indicating that the metal ion is not readily oxidized to the Co(III) state by dioxygen. The extinction coefficient for the protein-bound Co(II) is in the middle of the range characteristic of hexacoordinate Co(II). Five-coordinate Co(II) often shows additional bands around 600 nm. Since these are absent in Co(II)-soaked MMOH, the metal coordination in the enzyme appears to be distorted octahedral. The spectrum of $Co_2$−Hr displays a maximum at 519 nm with a very similar extinction coefficient of 34 $M^{-1}$ $cm^{-1}$ (Table 3) (*11*). Charge-transfer bands at 650 and 850 nm were also observed, however, leading to an assignment of a pentacoordinate Co(II) site (*11*). Binding of Co(II) to bacterioferritin gives rise to a spectrum with maxima at 520, 555, 600, and 625 nm with extinction coefficients ranging from 75 to 155 $M^{-1}$ $cm^{-1}$. This spectrum was interpreted as arising from pentacoordinate or pseudotetrahedral Co(II) (*9*). The Co(II) form of ribonucleotide reductase contains maxima at 515 and 550 nm with an $\epsilon_{550}$ of 115 $M^{-1}$ $cm^{-1}$ indicative of pentacoordination (*7*).

*Global Folds of Apo, Mn(II)-Soaked, and Co(II)-Grown MMOH.* Apo MMOH crystals were grown by using conditions similar to that for the holoprotein. The crystallization drops contained a substantial amount of heavy precipitate as compared to those observed for holo MMOH, which are typically free of aggregated protein. Crystals of apo MMOH diffracted on average to 2.3 Å versus 2.0 Å for the holoprotein and were roughly half the size (0.25 mm × 0.1 mm × 0.1 mm vs 0.5 mm × 0.3 mm × 0.08 mm). The addition of $CoCl_2$ to the crystallization solutions resulted in larger crystals, comparable in size to those of holo MMOH, which diffracted to 2.0−2.1 Å and had less precipitation. Well-diffracting crystals did not grow in the presence of $MnCl_2$. Instead, a heavy precipitate was generated. The Mn(II) form of MMOH was generated by soaking apo crystals with $MnCl_2$. Because of differences in the preparation of the Co(II)- and Mn(II)-substituted MMOH crystals,

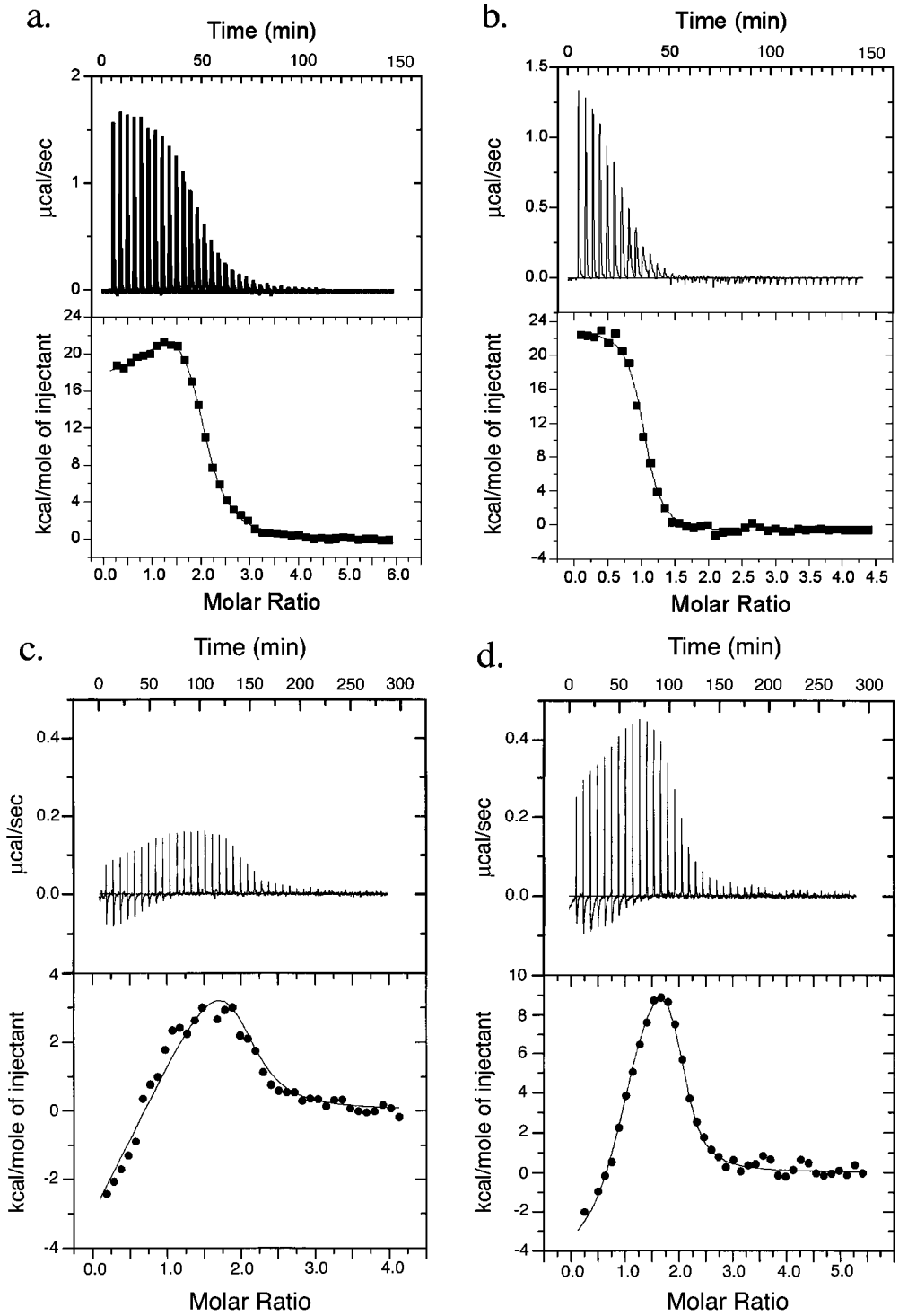


FIGURE 3: Isothermal titration calorimetry of MMOB and MMOD binding to holo and apo MMOH. MMOB was titrated to holo (a) and apo (b) MMOH as described in the text. The titrations of MMOD to holo and apo MMOH are depicted in panels c and d, respectively. The integrated data are also shown with fits to a sequential binding equation where $n = 2$. The binding constants are listed in Table 2.

Table 2: MMOB and MMOD Binding Constants for Apo and Holo MMOH

| sample | $K_{d1}$ ($\mu$M) | $K_{d2}$ ($\mu$M) |
|---|---|---|
| apo MMOH and MMOB | $0.21 \pm 0.027$ | $69 \pm 57$ |
| apo MMOH and MMOD | $0.027 \pm 0.0043$ | $0.29 \pm 0.032$ |
| holo MMOH and MMOB | $0.062 \pm 0.013$ | $0.70 \pm 0.035$ |
| holo MMOH and MMOD | $0.15 \pm 0.045$ | $0.63 \pm 0.16$ |

the final structures will be termed Co(II)-grown and Mn(II)-soaked MMOH, respectively. The observations made during the crystallization of the holo- and apoenzyme suggest that the apoprotein is prone to aggregation due to localized unfolding in the metal-coordinating four-helix bundle and that the addition of divalent metal ions such as Co(II) may help refold the protein. The CD spectra of apo and holo MMOH are identical, indicating the overall structure of MMOH in solution is perturbed very little by removal of its iron (Figure S2 of the Supporting Information).

The global structure of apo MMOH is similar to that of holo MMOH in both crystal forms I and II (*25*, *36*). Regions

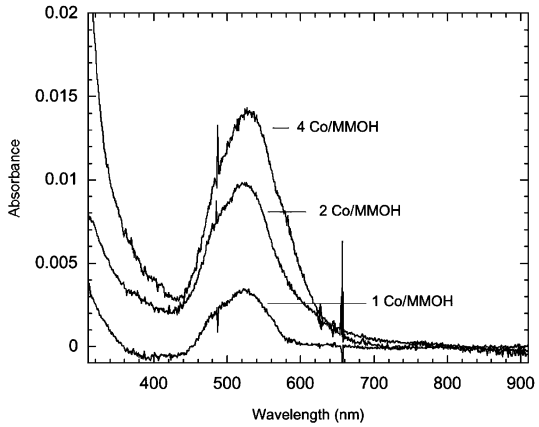


FIGURE 4: Optical difference spectra obtained by subtracting the spectrum of apo MMOH (105 $\mu$M) from that of apo MMOH in the presence of 1, 2, and 4 molar equiv of $CoCl_2$. Conditions are given in the text.

Table 3: Properties of Co(II)-Reconstituted Non-Heme Diiron Proteins

| | $\lambda_{max}$ (nm) | $\epsilon$ ($M^{-1}$ $cm^{-1}$) | predicted geometry | ref |
|---|---|---|---|---|
| methane monooxygenase | 520 | 35−40 | distorted octahedral | this work |
| hemerythrin | 519<br>650<br>850 | 34 | pentacoordinate | *11* |
| bacterioferritin | 520<br>555<br>600<br>625 | 75−155 | pentacoordinate/ pseudotetrahedral | *9* |
| ribonucleotide reductase R2 protein | 515<br>550 | 115 | pentacoordinate | *7* |

Table 4: Average *B*-Factors for Selected Regions of the MMOH α-Subunits[a]

| | $H_{red}$ | apo | Co(II) | Mn(II) |
|---|---|---|---|---|
| α-subunit | 28.0 | 41.7 | 37.1 | 42.8 |
| (residues 18−527) | 26.8 | 41.8 | 37.5 | 44.5 |
| residues 195−206 | 25.8 | 60.9 | 39.2 | 72.0 |
| (helix E) | 27.2 | 57.4 | 43.0 | 71.0 |
| residues 247−267 | 38.9 | 70.4 | 49.0 | 90.6 |
| (helix F) | 41.1 | 68.9 | 53.5 | 91.8 |
| residues 312−325 | 51.4 | 79.8 | 63.5 | 106.3 |
| (helix H) | 45.2 | 72.1 | 58.7 | 83.4 |
| average helices E, F, and H | 38.3 | 68.3 | 51.5 | 85.6 |
| (average for E, F, and H) − (average for α-subunit) | +10.9 | +26.5 | +14.2 | +42.0 |

[a] Units are in square angstroms. The average *B*-factors for each protomer in the $\alpha_2\beta_2\gamma_2$ dimer are presented. PDB entry 1FYZ was used to calculate the average *B*-factors for form II $MMOH_{red}$. Paired rows of numbers delineated by curly brackets refer to the two protomers of the MMOH dimer.

of the α-subunit, including portions of the diiron-containing four-helix bundle, however, are more disordered with higher average temperature factors (Table 4 and Figure 5a,b). The electron density for residues 195−206, 247−267, and 312−325, on helices E, F, and H, respectively, near the α-subunit−$\beta$-subunit interface is sparse and, for some residues, absent altogether. This result reflects disorder, as evidenced by higher average *B*-factors in these regions (68.3 Å$^2$) compared to the same regions in reduced MMOH (38.3 Å$^2$) and by the average *B*-factors for the α-subunits of holo MMOH (27.4 Å$^2$) and apo MMOH (41.7 Å$^2$). Except for the regions of helices E, F, and H mentioned above, the folds of the α-, $\beta$-, and $\gamma$-subunits appear to be unperturbed by the lack of iron. The same regions that are disordered in apo MMOH are even more so in Mn(II)-soaked MMOH. The relative thermolability of these regions increases on average from 42.0 to 85.6 Å$^2$ (Table 4 and Figure 5d). The only difference occurs for residues near the metal-binding center, which are ordered due to the presence of Mn(II). In the Co(II)-grown structure, helices E, F, and H are perfectly ordered and electron density is available for all of their residues. This observation is consistent with lower average *B*-factors and smaller discrepancies between the *B*-factors of the α-subunit and the regions of interest on helices E, F, and H.[3]

The "northern" end of the four-helix bundle is highly ordered in the apo, Mn(II), and Co(II) forms of MMOH. This ordering may reflect stability provided by the hydrogen bonding network behind the active site histidines that extends ~12−13 Å to the surface of the protein (*21*). In the apo and Mn(II) structures, electron density is available for all of these residues and their positions with respect to those in the $MMOH_{red}$ and $MMOH_{ox}$ structures are not perturbed (Figure S3 of the Supporting Information). In the apo RNR-R2 structure, a similar network remains intact (*6*).

*Active Sites of Apo, Mn(II)-Soaked, and Co(II)-Grown MMOH.* In the structure of apo MMOH, the metal-coordinating ligands at the active site demonstrate more flexibility (Figures 6 and 8a). Glu-209 and Glu-243, which form part of helices E and F, respectively, are partially disordered. The positions of Glu-114 and Glu-144 are similar to those observed in the holoprotein with the exception of the Glu-114 carboxylate group, which has rotated by 90° with respect to its position in the holoprotein to hydrogen bond to two water molecules modeled into the electron density among the four glutamates. The analogous residue in *E. coli* RNR-R2, D84, can adopt a conformation similar to that of Glu-114 in apo MMOH and coordinate to iron in a bidentate chelating or monodentate fashion, depending upon the oxidation state and preparation of the enzyme (*8*, *37*, *38*). The alternate conformation of the Glu-114 carboxylate in the apo structure suggests that second-shell coordination sphere constraints, originating from the protein to hold the carboxylate in place, are absent. Hydrogen bonding to the terminal water molecule on Fe1 in the oxidized and reduced forms of MMOH may dictate the typical monodentate coordination of Glu-114. Second-coordination sphere water molecules, however, also interact with the glutamate and the terminal water molecule in the different oxidized and reduced structures of MMOH. In the oxidized form, positional variations or the absence of these waters from one structure to the next makes them unlikely contributers to the stabilization of the Glu-114 geometry. In the reduced form, a water molecule consistently bridges the noncoordinating oxygen of Glu-114 and the amide backbone of Leu-110, but it is unknown whether this water has a significant impact on the conformation of this residue (*25*, *36*, *39*, *40*). Glu-144 of apo MMOH forms hydrogen bonds to both an active

[3] The crystal structures of Fe(II)- and Co(II)-soaked apo MMOH determined to 2.5 Å resolution exhibit disorder in helices E, F, and H similar to that of the Mn(II)-soaked apo MMOH.

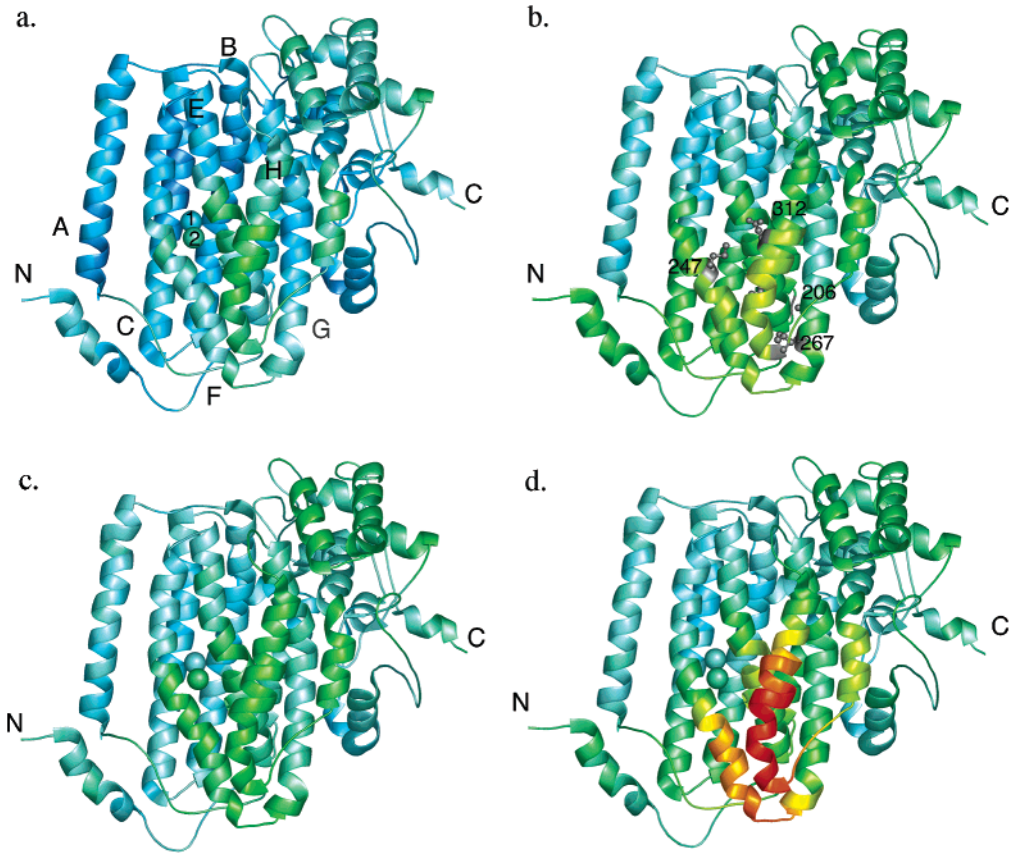


FIGURE 5: Structures of an α-subunit from each of the (a) Fe(II), (b) apo, (c) Co(II)-grown, and (d) Mn(II)-soaked forms of MMOH colored with respect to their *B*-factors. Blue represents a low level of disorder, whereas red represents a high level of thermal disorder. The α-helices (A−H) and metal ion positions (1 and 2) are labeled in panel a and are the same in all panels. The helix D label is occluded by the structure. The positions of residues marking the start or end of regions with poor electron density, as defined in Table 4, are presented in panel b. PDB entry 1FYZ was used to generate panel a. All figures using protein coordinates were generated by using PyMOL (*64*).

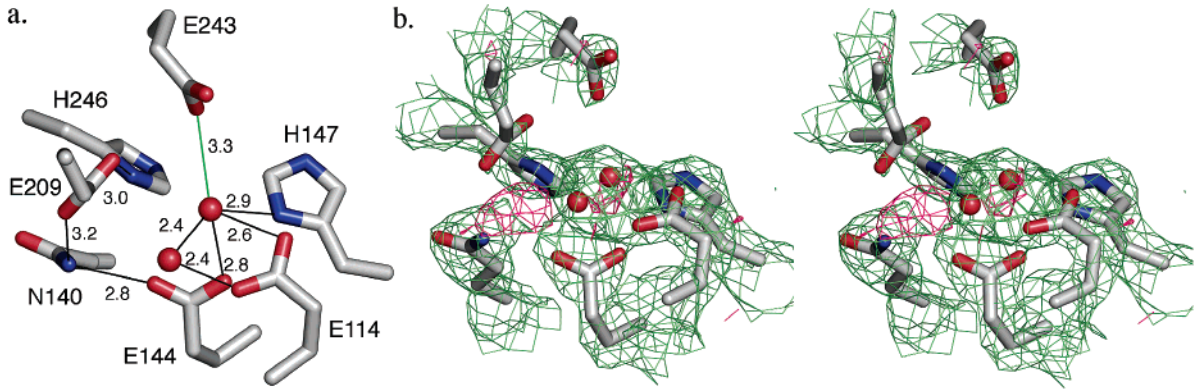


FIGURE 6: (a) Structure of the apo MMOH active site depicting hydrogen bonding patterns (black lines) and distances. A weak hydrogen bond is depicted as a green line. (b) Stereoview of the apo active site from protomer 1. The $|2F_o| - |F_c|$ electron density map (green) is contoured to $1\sigma$, and the $|F_o| - |F_c|$ map (pink) is contoured to $3\sigma$. Red spheres represent water molecules. The structure of the apo site from the second protomer is more disordered than the first, and therefore more difficult to model (not shown).

site water molecule and the amine moiety of Gln-140, the side chain of which has shifted slightly compared to its position in the holoprotein. The remaining metal-coordinating ligands, His-147 and His-246, are highly ordered. The His-246 side chain in apo MMOH shifts slightly toward the vacant Fe2 binding site yet, despite this shift, is still within hydrogen bonding distance of Asn-242. The position of His-147 is unperturbed in the apo structure.

The two water molecules are modeled into the electron density at the Fe1 binding position in the active site. These waters are 2.4 Å from each other and 2.5−3.0 Å from the carboxylate and histidine ligands. However, they cannot neutralize the overall four negative charges contributed by the glutamates in this buried region of the protein, nor do they account for all of the electron density in the area. Calcium, which is a major constituent of the MMOH crystallization buffer, could not be modeled successfully into this region. Attempts to do so at full occupancy resulted in unreasonable geometry and negative difference electron density artifacts. Given the overall disorder in the apo MMOH active site from both α-subunits, we cannot exclude the possibility that this site may be at least partially occupied by an adventitious cation like sodium, the presence of which would help to neutralize the buried charge. A hydronium

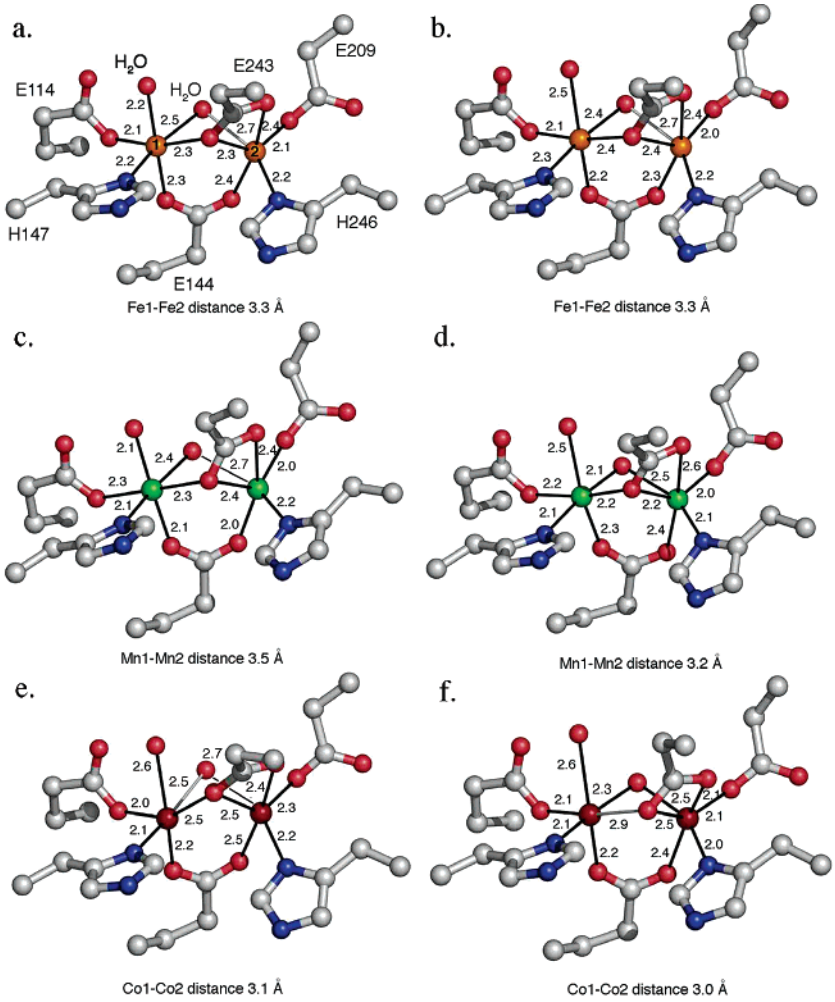


FIGURE 7: Structures of the MMOH active sites: (a) $MMOH_{red}$ protomer 1, (b) $MMOH_{red}$ protomer 2, (c) Mn(II) protomer 1, (d) Mn(II) protomer 2, (e) Co(II) protomer 1, and (f) Co(II) protomer 2. Panels b−f are labeled like panel a. Electron density contour plots for the Co(II) and Mn(II) active sites are depicted in Figure S3 of the Supporting Information.

ion ($H_3O^+$) or protonation of the histidines could also neutralize the charge. Since MMOH was crystallized at pH 7.0, however, the latter possibility is less likely. Between Glu-144 and Asn-140, there is a large feature of difference electron density. Again, because of the disorder within the region, it is unknown what atoms account for this electron density. In the absence of any definitive proof, we tentatively assign this density to water but recognize fully that a satisfactory solution is not at hand.

The Mn(II)-reconstituted active sites in each of the two α-subunits have metal−ligand distances and geometry similar to those in the chemically reduced forms of MMOH (Figure 7c,d and Figure S4 of the Supporting Information). The Mn−Mn distances lie between 3.2 and 3.5 Å depending on the protomer, but otherwise, the dimanganese and diiron forms of MMOH are isostructural (Figure 8b). The active site of Co(II)-grown MMOH is also similar to that of the chemically reduced native protein and Mn(II)-reconstituted MMOH except that the Co−Co distances are shorter, being 3.1 and 3.0 Å (Figures 7d,e and 8c). The pseudooctahedral geometry observed for both cobalt ions in both of the protomers is in accord with electronic spectral data on the Co(II)-reconstituted enzyme. The metal−ligand and metal−metal distances in the Mn(II) structure resemble more closely those found in $MMOH_{red}$. Comparison of the Mn(II), Co(II), and Fe(II) active sites reveals that Glu-209, Glu-243, and His-246 are the most flexible ligands, a feature that is perhaps required for accommodation of the varying metal−metal distances (Figure 8b,c). It is also of interest to note that the position of metal 1 does not vary among these structures whereas that of metal 2 does. Similar observations were made previously by comparing the oxidized, mixed-valent, and reduced forms of MMOH (*40*). As a result of the movements of metal 2 and its coordinating residues, the water molecule between the metals that extends into the active site pocket can adopt bridging, semibridging, and terminal coordination modes. The varied positions of this water molecule may be important for opening a coordination site for the reaction of dioxygen with one of the iron atoms (*39*).

Neither the dicobalt(II)- nor dimanganese(II)-reconstituted form of MMOH, in either the solution or crystalline state, was readily oxidized by air or hydrogen peroxide. Thus, the dicobalt(III) and dimanganese(III) forms were not investigated.

## DISCUSSION

*Effects of MMOB and MMOD on Binding of Iron to MMOH.* We have developed a new method for generating apo MMOH and can quantitatively observe its formation by monitoring the absorbance at 510 nm of $[Fe(o\text{-phen})_3]^{2+}$, which accumulates during the process. The rate constant for

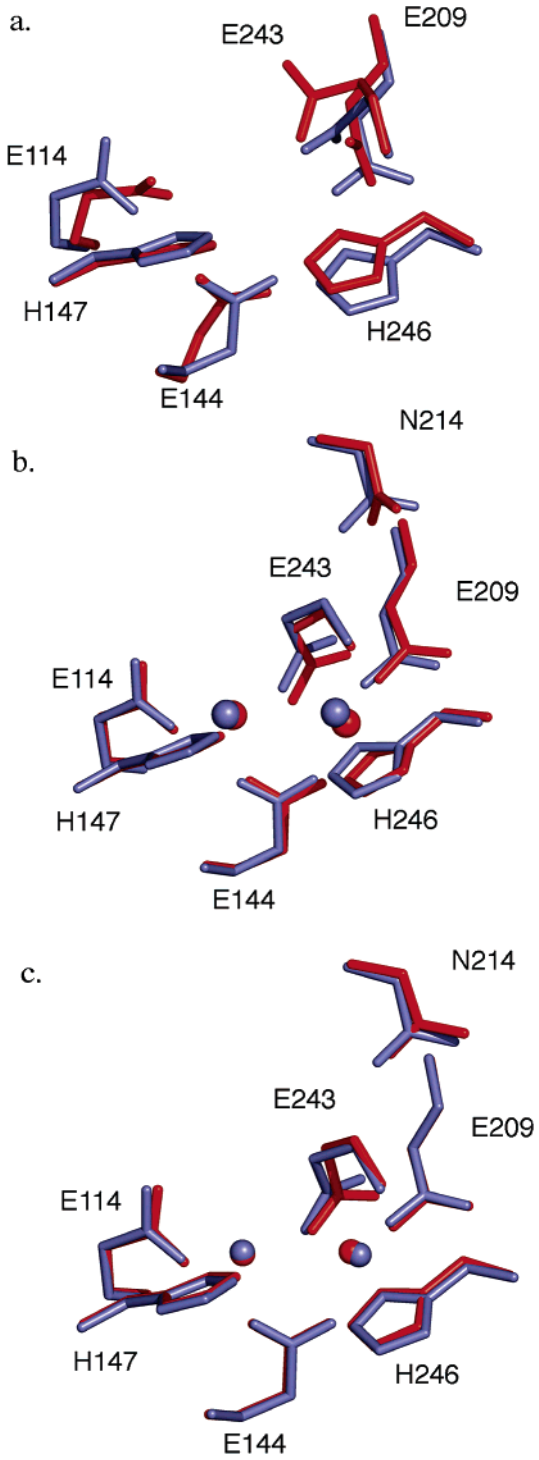


FIGURE 8: Superposition of the apo, Mn(II), and Co(II) forms of MMOH (red) with the native MMOH active sites (blue). (a) Apo vs oxidized MMOH (PDB entry 1FZ1). (b) Mn(II) vs reduced MMOH (PDB entry 1FYZ). (c) Co(II) vs reduced MMOH.

iron release from the protein is 1.6 $h^{-1}$, and this process is complete in just under 3 h. MMOB and MMOD significantly alter the kinetics of release of Fe(II) from MMOH, the rate constants being 0.07 and 0.11 $h^{-1}$, respectively. Removal of iron from the MMOB−MMOH and MMOD−MMOH complexes is estimated to take more than 40 h to complete. In crystal structures of reduced MMOH (*40*) and in Fe(II)-reconstituted apo MMOH (data not shown), the Fe2 metal binding site exhibited an excessively low occupancy, suggesting that Fe1 is the high-affinity metal binding site. For RNR-R2, however, the Fe2 site has the higher affinity (*41*). Preliminary attempts to determine by EPR whether metal binding to MMOH is cooperative, in the presence and absence of MMOB and MMOD, were made, but the data were inconclusive.

Previous iron reconstitution studies monitoring enzyme activity as a function of time demonstrated that MMOB slows the binding of Fe(II) to the active site (*3*). It is unknown at present whether MMOD alters the rate of iron uptake. From these results, we learn that MMOB and MMOD both decrease the relative $k_d$ values for iron release and that MMOB decreases the relative rate constant for iron uptake. The mechanism by which these proteins exert such an affect on MMOH remains to be determined.

MMOB and MMOD both bind to the surface of the α-subunit of MMOH (*3*, *42*), affect the spectroscopic and redox properties of the MMOH diiron center (*1*), stimulate (MMOB) or inhibit (MMOD) hydroxylase activity, and in the case of MMOB alter the product regioselectivity (*43*). How these proteins alter the structure of MMOH has been an important unanswered question about this class of multicomponent enzyme systems because detailed structures of the MMOH−MMOB and MMOH−MMOD complexes have not been determined. Recent saturation recovery EPR and chemical cross-linking data suggest that MMOB binds somewhere on helices E and F (*44*, *45*),[4] a result that is consistent with previous spectroscopic and biochemical findings. Moreover, biochemical investigations indicate that MMOB and MMOD compete with each other for the same binding site on MMOH (*3*).

In view of this minimal information about MMOB and MMOD docking, the iron release data presented here suggest that these proteins modulate the direct release of iron through the four-helix bundle by binding to the regions of helices E and F that are closest to the diiron center and physically disrupting conformational changes required for the exit of Fe(II). It is unlikely that the metal ions will traverse the three hydrophobic cavities in the core of the MMOH α-subunit to escape into the solvent (*46*). There is evidence to support a model whereby MMOB binding and MMOD binding rigidify the residues on helices E and F, limiting protein breathing within this region required for extrusion of Fe(II) to the solvent. Recent X-ray absorption spectroscopy (XAS) results indicate that MMOB decreases the thermal disorder of the outer shell scattering atoms near the diiron center.[5] It was concluded that binding of MMOB to $MMOH_{red}$ may serve to "organize" the diiron active site and the environment around it. Studies of the sMMO and toluene 4-monooxygenase (T4MO) regiospecific hydroxylations reveal a shift in product distributions in the presence of their respective regulatory proteins (*43*, *47*). If the regulatory protein from both enzyme systems binds to helices E and F, residues on these helices that help form the active site pocket, specifically, Ile-217, Thr-213, Gly-208, Leu-204, Phe-192, and Phe-188 in MMOH, must move when the hydroxylase−regulatory protein complex is formed. Mutagenesis and product distribution studies involving Thr-201 from T4MO,

[4] K. Zhu, M. H. Sazinsky, K. Zhu, E. Pozharski, K. V. Lakshmi, S. Riku, S. J. Lippard, and G. W. Brudvig, manuscript in preparation.

[5] D. Rudd Jackson, M. H. Sazinsky, S. J. Lippard, B. Hedman, and K. O. Hodgson, submitted for publication.

analogous to Thr-213 of sMMO, using different aromatic substrates strongly suggest that the regulatory protein directly influences the position of this absolutely conserved active site residue on helix E (*48*). Crystallographic studies of MMOH containing different bound product molecules demonstrate that residues 212−216 on helix E can undergo dramatic structural rearrangements and attest to the inherent flexibility of this region of the four-helix bundle.[6] In the absence of the regulatory protein, the substrate binding cavity and helices E and F can be considered to be in a relaxed state. When the regulatory protein is present, this region may become less flexible, enforcing specific product formation. Such enhanced rigidity close to the diiron center may slow the rates of uptake and release of Fe(II) by MMOH in the presence of MMOB. In addition to this mechanism, direct blocking of an exit pore may contribute to the kinetics of Fe(II) mobilization.

If the above interpretations are correct, the kinetic data on Fe(II) trafficking through MMOH in the presence of MMOB and MMOD also suggest that the binding of these proteins may limit solvent access to the diiron center. The crystal structure of the toluene/*o*-xylene monooxygenase hydroxylase (ToMOH), which has a diiron center geometry identical to that in MMOH, indicates that differences in the reactivity of sMMO and ToMO are based on the greater access of hydrocarbon substrates to the diiron center of the latter (*49*). Thus, the regulatory protein in these different multicomponent monooxygenase enzyme systems may also serve to gate access to the active sites from solvent, in addition to altering product regiospecificity, by controlling substrate access and altering the transfer of protons and electrons to the diiron centers. An MMOB quadruple mutant from *Methylosinus trichosporium* OB3b, in which surface residues N107, S109, S110, and T111 were mutated to either alanine or glycine, exhibited a 7-fold decrease in the rate of intermediate Q decay in the presence of methane and a 3-fold increase in Q reactivity toward the alternate substrates furan and nitrobenzene (*50*). On the basis of this finding, it was proposed that these mutations in MMOB, which essentially trim the topology of its surface, allow for increased solvent and substrate access to the MMOH active site. It was also proposed that the faster rate of Q decay for the MMOB quadruple mutant (0.12 $s^{-1}$) versus that of the wild-type protein (0.039 $s^{-1}$) in the absence of substrate, in addition to the 7-fold decrease in the rate of methane hydroxylation, could be due to enhanced solvent access. This concept of solvent penetration/protection would assign to MMOB another subtle, yet possibly important, function in addition to those suggested previously.

*Disorder within Helices E, F, and H.* Comparisons between the apo, Mn(II)-soaked, and Co(II)-grown MMOH structures reveal that metal binding to the four-helix bundle is essential for the proper folding of helices E, F, and H. The differences in the ordering of these helices in the Mn(II)-soaked and Co(II)-grown structures are striking. Why does the addition of Mn(II) to apo MMOH crystals fail to reorder the four-helix bundle when this region of the protein is not involved in crystal packing? One explanation may be that the apo MMOH crystals trap residues 195−206, 247−267, and 312−325 in a partially unfolded state, which upon addition of metal cannot refold. In contrast, solublized apo MMOH may have a higher degree of freedom than the crystalline form and can therefore refold properly to a "native-like" state before nucleation and crystal growth in the presence of metal ions. The observation that 80−90% of the sMMO hydroxylation activity is recovered by reconstituting apo MMOH with Fe(II) indicates that the apoprotein is not irreversibly trapped in an unfolded state. The fact that Co(II)-grown MMOH crystals contain properly refolded hydroxylase is consistent with the return of activity in Fe(II)-reconstituted MMOH.

The source of the disorder in helices E, F, and H is puzzling, for how does the absence of metal ions in the middle of a four-helix bundle translate to heavily disordered regions more than 20 Å away in the α-subunit near the α-subunit−*β*-subunit interface? One force driving the destabilization of helices E and F could be the proximity of the four potentially negatively charged carboxylates within a buried region of the protein. The repulsion of these charges, if uncompensated, may cause the disorder in Glu-209 and Glu-243 and result in an unwinding of their respective helices. No such effect was reported in the different crystal structures of apo ribonucleotide reductase, however (*6*, *14*). These proteins diffract to a similar resolution as apo MMOH and were crystallized at lower pH (6.0−6.5), near the p$K_a$ of histidine, the protonation of which can partially compensate for the negative charges in the active site. MMOH crystallizes at pH 7.0, making charge compensation by protonated histidines less likely. Moreover, hydrogen bonds were observed between the carboxylate groups in the apo RNR-R2 structures that may facilitate neutralization of the charge and better order the active site. No corresponding hydrogen bonding pairs could be delineated between the carboxylates in apo MMOH, especially since two of the four residues are disordered, but we do not rule them out.

Alternatively, the disorder may be due to destabilization of the second and third metal coordination spheres. Comparison of the structures of MMOH and ToMOH reveals that the conformations of two Fe2-coordinating glutamate residues in both proteins are stabilized by hydrogen bonding to Gln-140 and Glu-111, respectively (*49*). Each of these residues also participates in a local hydrogen bonding network involving nonconserved amino acid side chains and structural water molecules, which lead from the diiron center toward the α-subunit−*β*-subunit interface region of the four-helix bundle. In MMOH, removal of iron may destabilize these interactions and disrupt the protein fold. At present, there is no direct obvious structural correlation between demetalation of the enzyme and the disorder in helices E, F, and H 20 Å away from the active site.

The northern end of the four-helix bundle is highly ordered in the apo and Mn(II)-grown MMOH structures (Figure 5), presumably due to the hydrogen bonding network behind the diiron center that involves both coordinating histidines. A similar observation was made about the structure of apo RNR-R2 (*6*). On the basis of this finding, it was hypothesized that the active site of RNR-R2 is preorganized before iron is inserted. This network has subsequently been determined to be an essential pathway for electron transfer in RNR-R2 (*51*, *52*). By analogy, the hydrogen bonding network in MMOH, which is absolutely conserved in all known multicomponent monooxygenase families such as phenol hy-

[6] M. H. Sazinsky and S. J. Lippard, submitted for publication.

droxylases, toluene monooxygenases, and alkene monooxygenases (*21*), may be a part of the electron transfer pathway from the 2Fe−2S cluster in the reductase or Rieske protein to the diiron center of the hydroxylase. The proposed ∼13 Å electron transfer distance from the diiron center to the surface is consistent with the observation that most redox partners in metalloproteins typically fall within this distance (*53*). This emerging principle for electron transfer distances holds true for rubreyrthin and bacterioferritin, both of which have electron donor metallocofactors ∼14 Å behind the diiron center histidines that are incorporated into the fold of the protein (*54*, *55*). If our above hypothesis is correct, it can be surmised that these types of monooxygenases have evolved highly specific and highly rigid pathways for efficient electron transfer.

*Helical Disorder and the MMOB−MMOD Binding Site.* Isothermal titration calorimetry studies indicate that MMOB has a 3.4-fold higher affinity for $MMOH_{ox}$ than for apo MMOH and that MMOD has a 5.5-fold higher affinity for apo MMOH than for the native hydroxylase. Moreover, the dissociation constants reported in Table 2 indicate that, if MMOB and MMOD were together in solution, MMOB would bind preferentially to $MMOH_{ox}$ and MMOD would bind preferentially to apo MMOH. The differences in the binding affinities of MMOB and MMOD for oxidized and apo MMOH indicate that the apoprotein surface must be slightly different from that of the holoenzyme. Cross-linking and saturation recovery EPR studies place the MMOH−MMOB binding site on helices E and F of the α-subunit near the α-subunit−$\beta$-subunit interface (*44*, *45*).[4] The predicted MMOB binding surface on MMOH coincides well with the disordered regions of helices E, F, and H in the apo and Mn(II)-soaked structures of MMOH. Furthermore, MMOB and MMOD are likely to compete for the same binding region on the surface of the MMOH α-subunit (*3*). Since helices E, F, and H exhibit the only structural differences in the apo and Mn(II) structures, and the affinities of MMOB and MMOD for MMOH change depending upon the metalation state, the disordered regions in MMOH may therefore be highlighting the locations of the MMOB and MMOD docking sites. Investigations into the properties underlying the principles of protein−protein recognition indicate that binding faces are generally solvent accessible and highly flexible (*56*−*59*). The disordered regions on MMOH exhibit both properties, and their locations are consistent with biochemical and spectroscopic data placing MMOD and MMOB near the diiron center on this region of the four-helix bundle (*44*, *45*).[4]

*Structural Perturbations at the MMOH Dimetallic Center.* One reason for determining both metalated and demetaled structures of MMOH was to probe the active site and nearby surface of the protein for various structural perturbations that may shed light on the possible affects of MMOB on the properties of MMOH. Spectroscopic studies of the MMOH−MMOB complex from *M. capsulatus* (Bath) and *Me. trichosporium* OB3b indicate that the effects of MMOB are very subtle. Ligand field CD and MCD results for MMOH from *Me. trichosporium* OB3b suggest that MMOB alters the coordination environment of only one of the two iron atoms in the reduced protein (*60*). XAS spectra comparing $MMOH_{red}$ with $MMOH_{red}$ and MMOB are virtually identical, suggesting that MMOB exerts a very small structural effect on the diiron center geometry (*61*). From crystallographic work, it was surmised that Fe2 is the site most perturbed since it lies closer to the surface, changes positions in the oxidized, reduced, and mixed-valent structures of MMOH, and coordinates to amino acid residues on helices E and F that are more flexible according to the *B*-factors from the different MMOH crystal structures and positional changes in the different oxidation states (*25*, *36*, *40*, *62*). The Mn(II) and Co(II) structures presented here provide further crystallographic evidence supporting variability in the coordinating ligands and metal positions on the "Fe2" side of the active site. These findings also suggest that, as MMOH cycles though the reduced, peroxo, Q, and oxidized intermediates, Glu-209, Glu-243, and His-246 are most likely to shift to accommodate the range of Fe−Fe distances, from 2.6 to 3.6 Å. One interesting feature in the $MMOH_{red}$, Mn(II), and Co(II) structures is that the water molecule between the metal ions in the substrate-binding active site pocket varies between bridging, semibridging, and terminal coordination modes. Such a change in coordination may well explain the observed MCD and XAS results. The movement of this water molecule may be important for opening a coordination site where dioxygen can bind and react with one of the iron atoms (*39*). Presumably, the Fe2 site is most reactive toward dioxygen since the bridging water seems to favor binding to Fe1 in most cases. This observation is also consistent with DFT calculations detailing the reactions of $O_2$ with $MMOH_{red}$ (*63*).

## SUPPORTING INFORMATION AVAILABLE

Effect of iron concentration on the formation of active MMOH (Figure S1), CD spectra of apo and holo MMOH (Figure S2), and electron density maps of the active sites (Figures S3 and S4). This material is available free of charge via the Internet at http://pubs.acs.org.

## REFERENCES

1. Merkx, M., Kopp, D. A., Sazinsky, M. H., Blazyk, J. L., Müller, J., and Lippard, S. J. (2001) Dioxygen activation and methane hydroxylation by soluble methane monooxygenase: A tale of two irons and three proteins, *Angew. Chem., Int. Ed. 40*, 2783−2807.
2. Baik, M.-H., Newcomb, M., Friesner, R. A., and Lippard, S. J. (2003) Mechanistic studies on the hydroxylation of methane by methane monooxygenase, *Chem. Rev. 103*, 2385−2420.
3. Merkx, M., and Lippard, S. J. (2001) Why *orfY*? Characterization of MMOD, a long-overlooked component of the soluble methane monooxygenase from *Methylococcus capsulatus* (Bath), *J. Biol. Chem. 277*, 5858−5865.
4. Atta, M., Nordlund, P., Åberg, A., Eklund, H., and Fontecave, M. (1992) Substitution of manganese for iron in ribonucleotide reductase from *Escherichia coli*, Spectroscopic and crystallographic characterization, *J. Biol. Chem. 267*, 20682−20688.
5. Atta, M., Fontecave, M., Wilkins, P. C., and Dalton, H. (1993) Abduction of iron(III) from the soluble methane monooxygenase hydroxylase and reconstitution of the binuclear site with iron and manganese, *Eur. J. Biochem. 217*, 217−223.
6. Åberg, A., Nordlund, P., and Eklund, H. (1993) Unusual clustering of carboxyl side chains in the core of iron-free ribonucleotide reductase, *Nature 361*, 276−278.
7. Elgren, T. E., Ming, L.-J., and Que, L., Jr. (1994) Spectroscopic studies of Co(II)-reconstituted ribonucleotide reductase R2 from *Escherichia coli*, *Inorg. Chem. 33*, 891−894.
8. Högbom, M., Andersson, M. E., and Nordlund, P. (2001) Crystal structures of oxidized dinuclear manganese centres in Mn-substituted class I ribonucleotide reductase from *Escherichia coli*: carboxylate shifts with implications for $O_2$ activation and radical production, *J. Biol. Inorg. Chem. 6*, 315−323.
9. Keech, A. M., Le Brun, N. E., Wilson, M. T., Andrews, S. C., Moore, G. R., and Thomson, A. J. (1997) Spectroscopic studies

of cobalt(II) binding to *Escherichia coli* bacterioferritin, *J. Biol. Chem. 272*, 422−429.
10. Zhang, J.-H., and Kurtz, D. M., Jr. (1992) Metal substitutions at the diiron sites of hemerythrin and myohemerythrin: Contributions of divalent metals to stablility of a four-helix bundle protein, *Proc. Natl. Acad. Sci. U.S.A. 89*, 7065−7069.
11. Zhang, J.-H., Kurtz, D. M., Jr., Maroney, M. J., and Whitehead, J. P. (1992) Metal substitutions at the diiron site of hemerythrin. A dicobalt(II) derivative, *Inorg. Chem. 31*, 1359−1366.
12. Hill, R. B., Raleigh, D. P., Lombardi, A., and Degrado, W. F. (2000) *De novo* design of helical bundles as models for understanding protein folding and function, *Acc. Chem. Res. 33*, 745−754.
13. Maglio, O., Nastri, F., Pavone, V., Lombardi, A., and Degrado, W. F. (2003) Preorganization of molecular binding sites in designed diiron proteins, *Proc. Natl. Acad. Sci. U.S.A. 100*, 3772−3777.
14. Andersson, M. E., Högbom, M., Rinaldo-Matthis, A., Blodig, W., Liang, Y., Person, B.-O., Sjöberg, B.-M., Su, X.-D., and Nordlund, P. (2004) Structural and mutational studies of the carboxylate bridged cluster in iron-free ribonucleotide reductase R2, *Biochemistry 43*, 7966−7972.
15. Bernhardt, P. V., and Lawrance, G. A. (2004) in *Comprehensive Coordination Chemistry II* (McCleverty, J. A., and Meyer, T., Eds.) Vol. 6, pp 1−145, Pergamon Press.
16. Pecoraro, V. L., Gelasco, A., and Baldwin, M. J. (1995) in *Advances in Chemistry Series*, pp 265−301 American Chemical Society, Washington, DC.
17. Pecoraro, V. L., Baldwin, M. J., and Gelasco, A. (1994) Interaction of manganese with diooxygen and its reduced derivatives, *Chem. Rev. 94*, 807−826.
18. Stemmler, T. L., Sossong, T. M., Jr., Goldstein, J. I., Ash, D. E., Elgren, T. E., Kurtz, D. M., Jr., and Penner-Hahn, J. E. (1997) EXAFS comparison of the dimanganese core structures of manganese catalase, arginase, and manganese-substituted ribonucleotide reductase and hemerythrin, *Biochemistry 36*, 9847−9858.
19. Strand, K. R., Karlsen, S., and Andersson, K. K. (2002) Cobalt substitution of mouse R2 ribonucleotide reductase as a model for the reactive diferrous state, *J. Biol. Chem. 277*, 34229−34238.
20. Willems, J.-P., Valentine, A. M., Gurbiel, R., Lippard, S. J., and Hoffman, B. M. (1998) Small molecule binding to the mixed-valent diiron center of methane monooxygenase hydroxylase from *Methylococcus capsulatus* (Bath) as revealed by ENDOR spectroscopy, *J. Am. Chem. Soc. 120*, 9410−9416.
21. Coufal, D. E., Blazyk, J. L., Whittington, D. A., Wu, W. W., Rosenzweig, A. C., and Lippard, S. J. (2000) Sequencing and analysis of the *Methylococcus capsulatus* (Bath) soluble methane monooxygenase genes, *Eur. J. Biochem. 267*, 2174−2185.
22. Kopp, D. A., Gassner, G. T., Blazyk, J. L., and Lippard, S. J. (2001) Electron-transfer reactions of the reductase component of soluble methane monooxygenase from *Methylococcus capsulatus* (Bath), *Biochemistry 40*, 14932−14941.
23. Gibbs, C. R. (1976) Characterization and application of ferrozine iron reagent as a ferrous iron indicator, *Anal. Chem. 48*, 1197−1201.
24. Gassner, G. T., and Lippard, S. J. (1999) Component interactions in the soluble methane monooxygenase system from *Methylococcus capsulatus* (Bath), *Biochemistry 38*, 12768−12785.
25. Rosenzweig, A. C., Brandstetter, H., Whittington, D. A., Nordlund, P., Lippard, S. J., and Frederick, C. A. (1997) Crystal structures of the methane monooxygenase hydroxylase from *Methylococcus capsulatus* (Bath): Implications for substrate gating and component interactions, *Proteins 29*, 141−152.
26. Leslie, A. G. W. (1992) Recent changes to the MOSFLM package for processing film and image plate data, *Joint CCP4+ESF-EAMCB Newsletter on Protein Crystallography*, Number 26.
27. Otwinowski, Z., and Minor, W. (1997) HKL Suite of programs, *Methods Enzymol. 276*, 307−326.
28. Brünger, A. T., Adams, P. D., Clore, G. M., Delano, W. L., Gros, P., Grosse-Kunstleve, R. W., Jiang, J.-S., Kuszewski, J., Nilges, N., Pannu, N. S., Read, R. J., Rice, L. M., Simonson, T., and Warren, G. L. (1998) Crystallography and NMR system (CNS): A new software system for macromolecular structure determination, *Acta Crystallogr. D54*, 905−921.
29. McRee, D. E. (1999) XtalView/Xfit: A versatile program for manipulating atomic coordinates and electron density, *J. Struct. Biol. 125*, 156−165.
30. Laskowski, R. A., MacArthur, M. W., Moss, D. S., and Thorton, J. M. (1993) PROCHECK: A program to check the stereochemical quality of protein structures, *J. Appl. Crystallogr. 26*, 283−291.
31. Merkx, M., and Averill, B. A. (1998) $Ga^{3+}$ as a Functional Substitute for $Fe^{3+}$: Preparation and Characterization of the $Ga^{3+}$-$Fe^{2+}$ and $Ga^{3+}Zn^{2+}$ Forms of Bovine Spleen Purple Acid Phosphatase, *Biochemistry 37*, 8490−8497.
32. Liu, K. E., Valantine, A. M., Wang, D., Huynh, B. H., Edmondson, D. E., Salifoglou, A., and Lippard, S. J. (1995) Kinetic and spectroscopic characterization of intermediates and component interactions in reactions of methane monooxygenase from *Methylococcus capsulatus* (Bath), *J. Am. Chem. Soc. 117*, 10174−10185.
33. Green, J., and Dalton, H. (1988) The biosynthesis and assembly of protein A of soluble methane monooxygenase of *Methylococcus capsulatus* (Bath), *J. Biol. Chem. 263*, 17561−17565.
34. Banci, L., Bencini, A., Benelli, C., Gatteschi, D., and Zanchini, C. (1982) Spectral-structural correlations in high-spin cobalt(II) complexes, *Struct. Bonding 52*, 37−86.
35. Maret, W., and Vallee, B. L. (1993) Cobalt as a probe and label of proteins, *Methods Enzymol. 226*, 52−71.
36. Rosenzweig, A. C., Frederick, C. A., Lippard, S. J., and Nordlund, P. (1993) Crystal structure of a bacterial non-haem iron hydroxylase that catalyses the biological oxidation of methane, *Nature 366*, 537−543.
37. Logan, D. T., Su, X.-D., Åberg, A., Regnström, K., Hajdu, J., Eklund, H., and Nordlund, P. (1996) Crystal structure of reduced protein R2 of ribonucleotide reductase: The structural basis for oxygen activation at a dinuclear iron site, *Structure 4*, 1053−1064.
38. Nordlund, P., Sjöberg, B.-M., and Eklund, H. (1990) Three-dimensional structure of the free radical protein of ribonucleotide reductase, *Nature 345*, 593−598.
39. Rosenzweig, A. C., Nordlund, P., Takahara, P. M., Frederick, C. A., and Lippard, S. J. (1995) Geometry of the soluble methane monooxygenase catalytic diiron center in two oxidation states, *Chem. Biol. 2*, 409−418.
40. Whittington, D. A., and Lippard, S. J. (2001) Crystal structures of the soluble methane monooxygenase hydroxylase from *Methylococcus capsulatus* (Bath) demonstrating geometrical variability at the dinuclear iron active site, *J. Am. Chem. Soc. 123*, 827−838.
41. Bollinger, J. M., Jr., Chen, S., Parkin, S. E., Mangravite, L. M., Ley, B. A., Edmondson, D. E., and Huynh, B. H. (1997) Differential iron(II) affinity of the sites of the diiron cluster in protein R2 of *Escherichia coli* ribonucleotide reductase: Tracking the individual sites through the $O_2$ activation sequence, *J. Am. Chem. Soc. 119*, 5976−5977.
42. Fox, B. G., Liu, Y., Dege, J. E., and Lipscomb, J. D. (1991) Complex formation between the protein components of methane monooxygenase from *Methylosinus trichosporium* OB3b: Identification of sites of component interaction, *J. Biol. Chem. 266*, 540−550.
43. Froland, W. A., Andersson, K. K., Lee, S. K., Liu, Y., and Lipscomb, J. D. (1992) Methane monooxygenase component B and reductase alter the regioselectivity of the hydroxylase component-catalyzed reactions, *J. Biol. Chem. 267*, 17588−17597.
44. Brazeau, B. J., Wallar, B. J., and Lipscomb, J. D. (2003) Effector proteins from P450cam and methane monooxygenase: Lessons in tuning nature's powerful reagents, *Biochem. Biophys. Res. Commun. 312*, 143−148.
45. MacArthur, R., Sazinsky, M. H., Kühne, H., Whittington, D. A., Lippard, S. J., and Brudvig, G. W. (2002) Component B binding to the soluble methane monooxygenase hydroxylase by saturation recovery-EPR spectroscopy of spin-labeled MMOB, *J. Am. Chem. Soc. 124*, 13392−13393.
46. Whittington, D. A., Rosenzweig, A. C., Frederick, C. A., and Lippard, S. J. (2001) Xenon and halogenated alkanes track putative substrate binding cavities in the soluble methane monooxygenase hydroxylase, *Biochemistry 40*, 3476−3482.
47. Pikus, J. D., Studts, J. M., McClay, K., Steffan, R. J., and Fox, B. G. (1997) Changes in the regiospecificity of aromatic hydroxylation produced by active site engineering in the diiron enzyme toluene 4-monooxygenase, *Biochemistry 36*, 9283−9289.
48. Mitchell, K. H., Studts, J. M., and Fox, B. G. (2002) Combined participation of hydroxylase active residues and effector protein binding in a *para* to *ortho* modulation of toluene 4-monooxygenase regiospecificity, *Biochemistry 41*, 3176−3188.

49. Sazinsky, M. H., Bard, J., Di Donato, A., and Lippard, S. J. (2004) Structure of the toluene/*o*-xylene monooxygenase hydroxylase from *Pseudomonas stutzeri* OX1: Substrate channeling and active site tuning of multicomponent monooxygenases, *J. Biol. Chem. 279*, 30600−30610.
50. Wallar, B. J., and Lipscomb, J. D. (2001) Methane monooxygenase component B mutants alter the kinetic steps throughout the catalytic cycle, *J. Am. Chem. Soc. 40*, 2220−2233.
51. Baldwin, J., Krebs, C., Ley, B. A., Edmondson, D. E., Huynh, B. H., and Bollinger, J. M., Jr. (2000) Mechanism of rapid electron transfer during oxygen activation in the R2 subunit of *Escherichia coli* ribonucleotide reductase. 1. Evidence for a transient tryptophan radical, *J. Am. Chem. Soc. 122*, 12195−12206.
52. Krebs, C., Chen, S., Baldwin, J., Ley, B. A., Patel, U., Edmondson, D. E., Huynh, B. H., and Bollinger, J. M., Jr. (2000) Mechanism of rapid electron transfer during oxygen activation in the R2 subunit of *Escherichia coli* ribonucleotide reductase. 2. Evidence for and consequences of blocked electron transfer in the W48F mutant, *J. Am. Chem. Soc. 122*, 12207−12219.
53. Page, C. C., Moser, C. C., and Dutton, P. L. (2003) Mechanism for electron transfer within and between proteins, *Curr. Opin. Chem. Biol. 7*, 551−556.
54. deMare, F., Kurtz, D. M., Jr., and Nordlund, P. (1996) The structure of *Desulfovbrio vulgaris* rubrerythrin reveals a unique combination of rubredoxin-like FeS4 and ferritin-like diiron domains, *Nat. Struct. Biol. 3*, 539−546.
55. Frolow, F., Kalb, A. J., and Yariv, J. (1994) Structure of a unique two fold symmetric haem-binding site, *Nat. Struct. Biol. 1*, 453−460.
56. Sundberg, E. J., and Mariuzza, R. A. (2000) Luxury accommodations: The expanding role of structural plasticity in protein−protein interactions, *Structure 8*, R137−R142.
57. Lo Conte, L., Chothia, C., and Janin, J. (1999) The atomic structure of protein−protein recognition sites, *J. Mol. Biol. 285*, 2177−2198.
58. Jones, S., and Thorton, J. M. (1996) Principles of protein−protein interactions, *Proc. Natl. Acad. Sci. U.S.A. 93*, 13−20.
59. DeLano, W. L., Ultsch, M. H., de Vos, A. M., and Wells, J. A. (2000) Convergent solutions to binding at a protein−protein interface, *Science 287*, 1279−1283.
60. Pulver, S. C., Froland, W. A., Lipscomb, J. D., and Solomon, E. I. (1997) Ligand field circular dichroism and magnetic circular dichroism studies of component B and substrate binding to the hydroxylase component of methane monooxygenase, *J. Am. Chem. Soc. 119*, 387−395.
61. Dewitt, J. G., Rosenzweig, A. C., Salifoglou, A., Hedman, B., Lippard, S. J., and Hodgson, K. O. (1995) X-ray absorption spectroscopic studies of the diiron center in methane monooxygenase in the presence of substrate and the coupling protein of the enzyme system, *Inorg. Chem. 34*, 2505−2515.
62. Elango, N., Radhakrishnan, R., Froland, W. A., Wallar, B. J., Earhart, C. A., Lipscomb, J. D., and Ohlendorf, D. H. (1997) Crystal structure of the hydroxylase component of methane monooxygenase from *Methylosinus trichosporium* OB3b, *Protein Sci. 6*, 556−568.
63. Gherman, B. F., Baik, M.-H., Lippard, S. J., and Friesner, R. A. (2004) Dioxygen activation in methane monooxygenase: A theoretical study, *J. Am. Chem. Soc. 126*, 2978−2990.
64. DeLano, W. L. (2002) *PyMOL*, DeLano Scientific, San Carlos, CA.

BI048140Z